Characterizing the Water Forming Reaction on Graphite and Ceria Supported Palladium Nanoparticles and Nanoislands by the Work Function

Baptiste Chatelain, Ali El Barraj, Carine Laffon, Philippe Parent, Clemens Barth

Characterizing the Water Forming Reaction on Graphite and Ceria Supported Palladium Nanoparticles and Nanoislands by the Work Function

Baptiste Chatelain, Ali El Barraj, Carine Laffon, Philippe Parent, and Clemens Barth*

Aix-Marseille University, CNRS, CINaM UMR 7325, 13288 Marseille, France

E-mail: clemens.barth@cnrs.fr

*To whom correspondence should be addressed

Abstract

The water forming reaction (WFR) between oxygen and hydrogen on metal surfaces is an important reaction in heterogeneous catalysis. Related research mostly focused on crystalline metal surfaces and thick films, however, supported nanoparticles (NP) have been rarely considered as well as a possible influence of the support on the NP catalytic activity. Here, we report on the WFR on graphite supported palladium NPs and nanoislands (NI), which are characterized at room temperature and under ultra-high vacuum conditions (UHV) by scanning tunneling microscopy (STM), noncontact atomic force microscopy (nc-AFM), Kelvin probe force microscopy (KPFM) and X-ray photoemission spectroscopy (XPS). We show that during the first cycles of sequential O_2 and H_2 pulses, atomic H reacts off preadsorbed atomic O, which can be followed by KPFM via monitoring the change of work function (WF) at the NPs and NIs. However, after a few WFR cycles, the WF changes get smaller and the mean WF of the Pd increases due to an irreversible deactivation of the catalyst: a filament structure is formed on the facets by O and C, which the latter gets probably released from the graphite during the WFR. In strong contrast to the Pd/graphite catalyst, the WFR can be followed without any changes during an unlimited amount of cycles on a carbon-free Pd/cerium oxide/Cu(111) catalyst, which clearly shows that the support plays a role in the WFR on nanometer sized Pd catalysts.

INTRODUCTION

Since its discovery in 1823 by J. W. Döbereiner[1,2], the water forming reaction (WFR) from gaseous oxygen and hydrogen on a platinum-group metal surface is a fundamental reaction in heterogeneous catalysis. The WFR can be a sub-reaction in a larger catalytic reaction (e.g., in the methane oxidation[3]) and finds a potential application in, e.g., hydrogen control systems of nuclear power plants[4]. Apart from Pt(111)[2,5,6], Ru(0001)[7] and Pd(001)[8,9], the WFR was studied in particular on Pd(111) by several surface science techniques such as molecular beam techniques[10], mass spectrometry[11,12], time-of-flight spectroscopy (TOF)[13],

thermal desorption spectroscopy (TDS)[11,14] and scanning tunneling microscopy (STM)[15,16]. Apart from crystalline Pd surfaces, polycristalline[17,18] and thick Pd films forming a metal-oxide-semiconductor (MOS) device[19,20] were used as well, and theory was used to explain the precise reaction pathways in general[3,21,22].

As shown on Pd, the WFR proceeds mostly over a Langmuir–Hinshelwood mechanism at low[10,11,14,20] and high pressures[4,12]: both molecular species adsorb dissociatively even at room temperature (RT) and combine to H_2O, which leaves the metal surface even below RT[10,11,15]. Although an early work does not exclude that the WFR may also proceeds directly via adsorbed H_2 [$H_2\,(\mathrm{ad}) + O\,(\mathrm{ad}) \rightarrow H_2O\,(\mathrm{g})$][14], all other work assumes that H_2 and O_2 are first adsorbed dissociatively[23,24] and form surface hydroxyls in a first step [$H\,(\mathrm{ad}) + O\,(\mathrm{ad}) \rightarrow OH\,(\mathrm{ad})$][10,20]. In the next water-forming step, experimental work assumes a hydrogen addition reaction [$OH\,(\mathrm{ad}) + H\,(\mathrm{ad}) \rightarrow H_2O\,(\mathrm{g})$][10] whereas theory predicts that rather two OH species form H_2O [$2\,OH\,(\mathrm{ad}) \rightarrow H_2O\,(\mathrm{g}) + O\,(\mathrm{ad})$][3,21] with the hydrogen addition reaction being important rather at higher temperatures[21].

In contrast to all the work done with bulk Pd samples and some work done with gas-phase clusters[25], only a limited amount of work can be found that deals with supported nanoparticles (NP)[4,26]. Independent from their general importance in catalysis, it is worth to study PdNPs and the WFR due to a potential influence of the support: for instance, carbon supports, which are frequently used in catalysis, get etched by PdNPs such that C is included into the NPs. This has been observed during the UHV growth of PdNPs on the HOPG surface already at moderate temperatures (150 °C)[27]. Such a*d*sorbed or a*b*sorbed C could change the reaction properties, leading, e.g., to the well-known phenomena of catalyst deactivation[28,29].

In this work we focus on the WFR at RT and under UHV conditions on PdNPs and Pd nanoislands (PdNIs), which are grown in their (111) epitaxy on highly oriented pyrolytic graphite (HOPG) and on ultra-thin cerium oxide (ceria) films on Cu(111) at 500 °C (PdNPs) and at RT (PdNIs). STM and noncontact atomic force microscopy (nc-AFM) are used to

study the surface morphology whereas STM allows obtaining atomic details on the palladium facets. Kelvin probe force microscopy (KPFM) is used to monitor the surface WF, which changes during a WFR. In particular KPFM is a suitable technique to study the WFR: (i) the WFR takes place at RT so that the reaction can be followed with an AFM that works at RT. (ii) The saturated (2×2) adsorption structure of atomic O[30–32] strongly increases the WF of Pd(111) by $+0.6\,\mathrm{eV}$[33–35] whereas saturated atomic H increases the WF by maximal $+0.16\,\mathrm{eV}$ at $p_{\mathrm{H2}} = 5 \times 10^{-7}\,\mathrm{mbar}$[23]. This means that a removal of O by H should therefore be visible by a large contrast change of some hundreds of millivolts in the KPFM image. (iii) Depending on the C state (amorphous C or graphene) on PdNPs/HOPG, the WF decrease induced by C can be eventually distinguished from the WF increase induced by adsorbed H and O[27,35]. (iv) With respect to Pd/HOPG, oxygen, hydrogen, water and other gases do not adsorb on the HOPG terraces at RT[36], so that the HOPG terraces always remain at their well-defined WF and therefore function as a reference surface for KPFM.

METHODS

A detailed description of our STM, nc-AFM, KPFM and XPS instruments as well as a description of the sample preparation and material properties (absolute WF values and lattice constants for Pd and HOPG) can be found in the Supporting Information. Here, we summarize the most important details.

Scanning Probe Microscopy (SPM). STM, frequency modulated nc-AFM and KPFM are performed at RT in an UHV chamber with a base pressure kept at $1 \times 10^{-10}\,\mathrm{mbar}$. KPFM is used in the frequency modulation mode[37] and applied during the nc-AFM imaging in the constant $\triangle f$ mode. During the scanning of the surface, the electrostatic tip-surface interaction is minimized at each image point by the sample bias voltage (tip at ground), yielding the contact potential difference (CPD) between tip and surface given by $\mathrm{CPD} = (\phi_{\mathrm{sample}} - \phi_{\mathrm{tip}}) / e$. An image of the CPD is simultaneously obtained with the topography nc-AFM

image whereas we call the CPD image *the work function image* for simplicity. If the tip-surface convolution effect in KPFM is small, the contrast of a WF image is directly related to WF differences on the surface. If the convolution is strong, measured WF differences are smaller than the true WF differences due to the tip averaging effect. A bright yellow/orange contrast in WF images corresponds to a relatively high WF whereas a dark blue/violet contrast corresponds to a relatively low WF. Note that because the AFM tips have been exposed to O_2 and H_2 prior to all experiments shown here, the tip's WF does not change when dosing O_2 and H_2. For more details see the Supporting Information and the one of Ref. [35].

Photoemission Spectroscopy (XPS). X-Ray photoelectron spectroscopy (XPS) is accomplished in a second UHV chamber with the Mg K_α radiation (1253.6 eV) delivered by an unmonochromatized X-ray source operated at 140 W. Photoelectron spectra are recorded with a hemispherical analyzer with 5-channel detection, using a pass energy of 50 eV for the survey spectrum and 20 eV for detail spectra. All XPS spectra are taken with the sample kept at RT.

Sample preparation. Clean HOPG supports are prepared by cleaving HOPG in air with an adhesive tape and by a following annealing between 650 and 800 °C in UHV during several hours. Ultra-thin ceria films are grown on a Cu(111) support by oxidizing a previously evaporated Ce film in 5×10^{-7} mbar O_2 at 550 °C[38]. The nominal thickness is about 3 to 4 monolayers (ML) whereas one ML is defined as the thickness of the repeating unit along the [111] direction, namely an O-Ce-O trilayer with a height of $h_{\mathrm{ML}} = a_{\mathrm{CeO2}}/\sqrt{3} \approx 3.12 \pm 0.01$ Å[39]. The PdNPs and PdNIs are grown separately in each of the two UHV chambers by evaporating neutral Pd atoms onto the sample surface. The support is kept at 500 °C and RT during the growth, which leads to PdNPs and PdNIs, respectively (see Figure 1). For the SPM and XPS experiments, same HOPG samples are used, which are always cleaved in air if a new HOPG surface is needed.

O_2 + H_2 Dosage Experiments. In each of the two UHV chambers, only a turbo molecular pump is used to keep the partial O_2 or H_2 pressure constant whereas ion getter

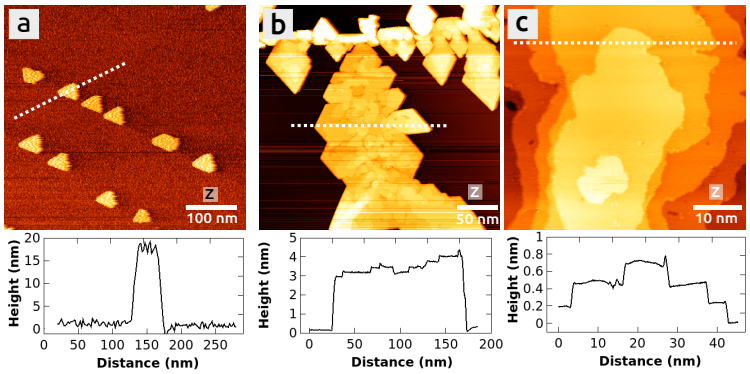

Figure 1: STM topography images of PdNPs (a) and PdNIs (b,c) after their growth in UHV at 500 °C and RT, respectively. Depending on the HOPG step density, the coverage of the HOPG surface by the PdNPs (5 % in (a)) strongly varies on the surface whereas the coverage of 35 % in (b) is found almost everywhere on the surface. Growth: 2.0 ML Pd at 500 °C + 30 sec long post-annealing at 500 °C (a) and 3.3 ML Pd at RT (b,c), STM: I = 0.20 (a), 0.63 (b) and 0.12 nA (c), U_{Bias} = + 4.2 (a), +0.66 (b) and +0.10 V (c), v = 2.0 (a,c) and 1.0 Hz (b).

and non-evaporable getter (NEG) pumps are separated from the main UHV parts by gate valves. The UHV chamber is back-filled with either O_2 or H_2 via leak valves at a chosen partial pressure, whereas the dosage is determined by the exposure time. Note that the real pressure in the tip-surface cavity is smaller than monitored by the gauge controller because of the small cavity size. Because the geometric correction factor is unknown, the relative sensitivity factors for O_2 and H_2 as given in, e.g., Ref. [40] (O_2: 0.87 and H_2: 0.44), are not accounted for. Here, we merely mention the reading from the controller of the pressure gauge and refer to the effective values if needed.

To reduce the complexity of the WFR during a simultaneous exposure of O_2 and H_2, both gases are sequentially dosed in the experiments as exemplified for a SPM experiment on a PdNI in Figure 2a (scanning from the bottom to the top): a part of the HOPG surface and the PdNI is first imaged under best UHV pressure conditions to obtain WF values of the clean as-prepared surface (bottom). Because the WF values of HOPG and Pd are different ($\phi_{HOPG,lit} = 4.5 \pm 0.1$ eV, $\phi_{Pd,lit} = 5.6 \pm 0.1$ eV, see Table S1 and S2 in the Supporting

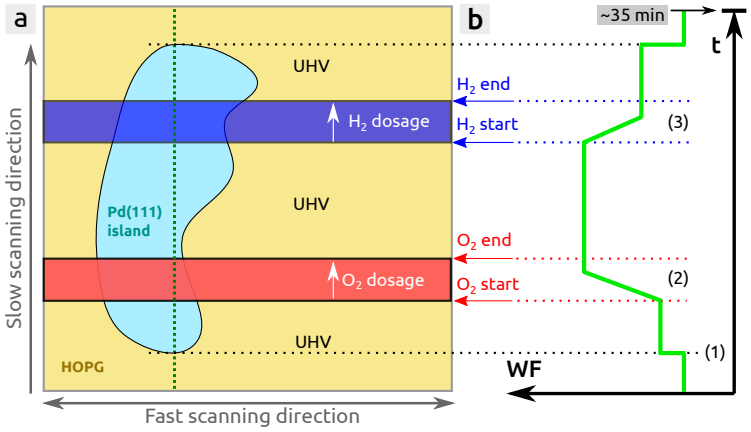

Figure 2: The experimental protocol for KPFM adsorption, desorption and reaction experiments based on sequential pulses of O_2 and H_2. (a) Sketch of a KPFM image, showing the HOPG support (yellow) and a PdNI (light blue) as well as a O_2 (red) and H_2 pulse (blue). The scanning proceeds horizontally (fast scanning direction, in forward and backward direction) from the bottom to the top (slow scanning direction). (b) Exemplifying profile taken at the green dotted line in (a) showing the expected WF difference between Pd and HOPG (1), and the expected WF increase and decrease upon an O_2 (2) and following H_2 pulse (3), respectively.

Information), the WF increases when the tip passes over the PdNI ((1) in Figure 2b). The sample is then exposed to a some seconds long pulse of O_2 and H_2 ((2) and (3) in Figure 2b). A pressure of $\sim 5 \times 10^{-7}$ mbar is chosen such that a dosage of one Langmuir (L) is reached within only about one scanning line during the scanning. Any possible changes in the WF can then be assigned to the action of either oxygen or hydrogen whereas the influence of other residual gases such as CO are kept small (see Supporting Information). After an O_2 or H_2 pulse, the gate valve of the ion getter and NEG pumps is immediately opened so that the residual pressure quickly decreases into the lower 10^{-10} mbar pressure range within ten seconds only. Therefore, almost no chemical surface reactions take place on the surface with the residual gas after a pulse has been sent. As discussed in this work, the WF varies upon the exposure of O_2 and H_2 pulses (see positions (2) and (3) in Figure 2b).

Note that a delivered O_2 or H_2 pulse only covers a few scanning lines of the 512×512 pixel^2 large image and is much thinner than shown in Figure 2a. The region between two pulses (yellow) is then obtained under best UHV conditions.

The same type of sequential dosage experiments are done in XPS studies, however, XPS is used only before and after all O_2 and H_2 pulses have been executed.

RESULTS

$O_2 + H_2$ exposure on PdNPs/HOPG. Figure 3a shows the topography (top) and WF image (bottom) of PdNPs after a growth of 2.0 monolayer (ML) Pd on HOPG at 500 °C. One ML is defined as the thickness of one atomic Pd layer, which is repeated along the [111] direction perpendicular on the surface, with a height of $h_{Pd(111)} = a_{Pd} / \sqrt{3} \approx 2.25$ Å (lattice constant a_{Pd}: see Table S3 in the Supporting Information).

Due to a relative strong tip-surface convolution effect, the NPs appear two times larger than in corresponding STM images obtained with the same tip (compare with Figure 1a and see Figure S1 in the Supporting Information). Owing to their 3D shape of a top-truncated

tetrahedron, the NPs exhibit well-known shapes from triangles to hexagons via various truncated shapes, with the NP's edges forming always angles of 60° and 120°[41]. The top facets are atomically flat and are in their (111) surface orientation, with the side facets having (111) and (001) orientations[27]. The NPs are attached at steps of the HOPG surface and have side lengths, which can vary between 10 and 30 nm, whereas the NP height can generally reach 15 nm and more (Figure 1a).

The corresponding WF image in Figure 3a shows bright NPs with a WF difference of up to $+0.3$ eV, which is typical for such NPs on HOPG[27,35]: the value is well below the expected WF difference of $\triangle\phi_{\text{Pd-HOPG}} = \phi_{\text{Pd}} - \phi_{\text{HOPG}} \approx +1.1$ eV between pristine Pd(111) and HOPG ($\phi_{\text{HOPG,lit}} = 4.5 \pm 0.1$ eV, $\phi_{\text{Pd,lit}} = 5.6 \pm 0.1$ eV, see Table S1 and S2 in the Supporting Information) because C is occupying subsurface sites in the NP and reducing the WF of the PdNPs[27].

In the following measurement (Figure 3b), the NPs are first imaged in UHV in the lower part of the image and the surface is then exposed to a 11.4 L short O_2 pulse (red arrow at the bottom). Note that the pulse only covers about 7 scanning lines in the 512×512 pixel^2 sized image so that the pulse length as such is not visible in the image. In other words, the surface regions between two pulses are always imaged under best UHV conditions ($\sim 10^{-10}$ mbar). Note also that the pressure and related dosage values have to be corrected by the relative sensitivity factors (O_2: 0.87, H_2: 0.44)[40]. However, the resulting dosage values (O_2: 13.1 L, H_2: 25.9 L) are sufficiently high to saturate the surface by one layer of oxygen[33] and hydrogen, respectively (see Discussion section).

As it can be also seen in the corresponding profile 1 (red) below the WF image, the WF of the NP increases by $+0.3$ eV upon the O_2 pulse. The increase of the WF is in agreement with previous observations[35]: during the pulse, oxygen dissociatively adsorbs on the PdNPs increasing the WF of the palladium. The increase here is smaller than the previously observed one ($+0.6$ eV[35]), which is due to the strong tip-surface convolution effect mentioned above. Note that, so far, we only focus on the qualitative trend of WF changes and do not consider

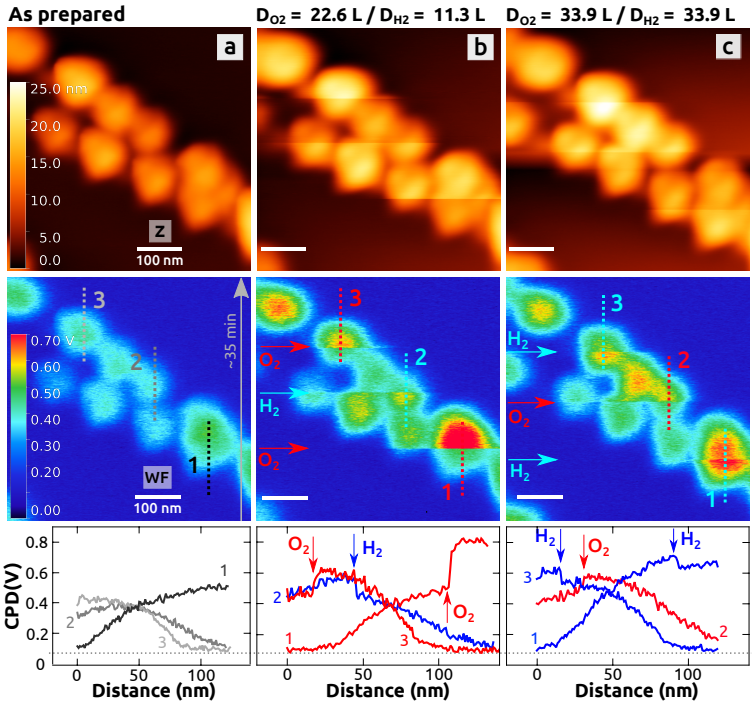

Figure 3: The WFR on PdNPs/HOPG, with KPFM experiments acquired before (a) and during the reaction (b,c). The topography (z) and WF images are shown on the top and in the middle row, respectively. The WF (z) images have all the same color and WF (nm) scale. The arrows in the WF images show the respective O_2 and H_2 pulses ($\sim 5.0 \times 10^{-7}$ mbar, 30 sec $\rightarrow \sim 11.3$ L) whereas the total dosages D_{O2} (D_{H2}) after each measurement are mentioned for O_2 (H_2) on the top. Underneath the WF images, typical color coded profiles taken at the respective colored dotted lines in the WF images are shown. All profiles have a number, which has the same color code. Vertical red and blue arrows in the profiles show the WF changes upon the O_2 and H_2 pulses, respectively. PdNP growth: 2.0 ML Pd at 500 °C + 30 sec post-annealing in UHV at 500°C, nc-AFM: $\triangle f$ = -9.5 (a,b) and -11 Hz (c).

absolute values.

After half of the image, a 11.3 L short H_2 pulse is sent (blue arrow in Figure 3b). The WF decreases by about -0.2 eV and remains constant afterwards in UHV (blue profile 2). A following O_2 pulse on the top (red profile 3) increases again the WF, this time by +0.2 eV. In the following, successively recorded measurement (Figure 3c), the order of the pulses with same strength (11.3 L) is reversed: first a H_2 then an O_2 pulse is sent at the same places of the previous image, with a last H_2 pulse on the top of the image. As a result, the WF decreases upon the first H_2 pulse whereas it increases upon the following O_2 pulse. The last H_2 pulse decreases again the WF.

As explained in the discussion section (see below), the WF changes that appear after the O_2 and H_2 pulses can be assigned to the WFR. Important to note is that the relative WF changes are much smaller in the second measurement in Figure 3c (-0.06, +0.05 and -0.08 eV) and that the final WF state of the NPs exhibits a mean WF of the PdNPs that is by up to $\sim$+0.2 eV higher than the mean WF of the initial state in Figure 3a (see Figure S2a,b in the Supporting Information).

$O_2 + H_2$ exposure on PdNIs/HOPG. To obtain more reliable values for the WF changes with almost no tip-surface convolution effect and to exclude a possible influence of the PdNP subsurface carbon on the WF changes, we consider measurements obtained on PdNIs: Figure 1b and also Figure S3 in the Supporting Information show PdNIs after the growth of 3.3 ML of Pd on a second clean HOPG surface at RT: such islands can reach lateral sizes of up to 300 nm, cover about 35% of the surface and exhibit a height between 2.5 and 3.5 nm. Furthermore, they are well separated from equally wide regions of clean HOPG. The main edges of the islands form angles of 120° or 60°, which is due to the (111) orientation of the top facets of the islands. On the top facets, several terraces can be found that exhibit integer step heights of the Pd(111) ML height whereas the steps are rather curved (Figure 1c) compared to the straight main edges of the islands (Figure 1b).

Because the PdNIs are grown at RT, there is no carbon that is included during the growth

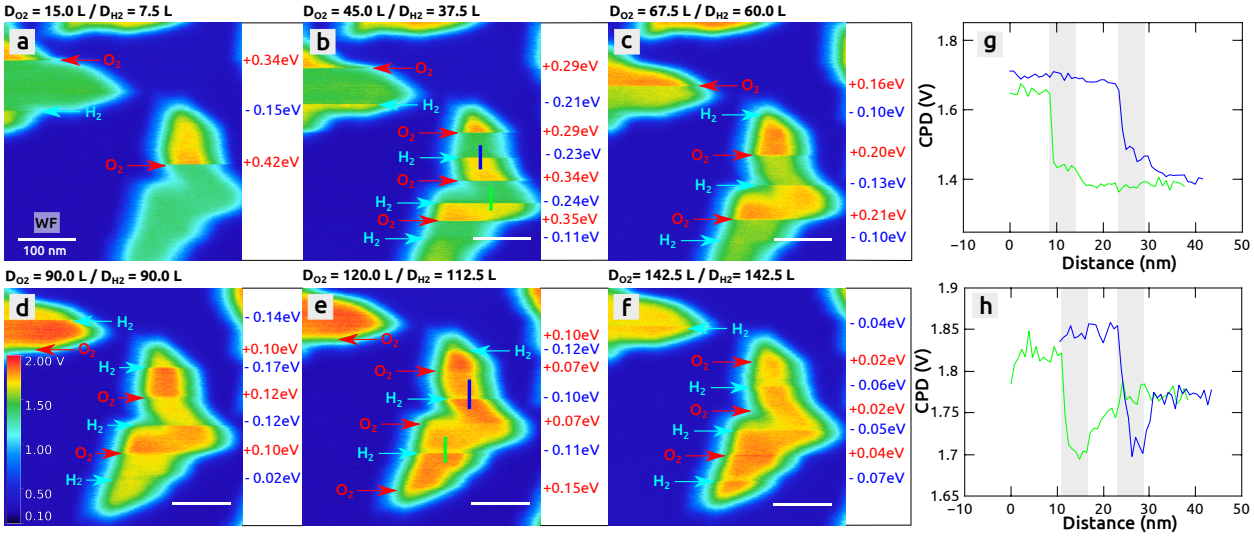

Figure 4: The WFR on PdNIs/HOPG during the acquisition of several consecutively recorded KPFM measurements (a-f). Only WF images are shown, which all have the same color and WF scale. The arrows show the respective O_2 and H_2 pulses (one pulse: $\sim 5.0 \times 10^{-7}$ mbar, 20 sec $\rightarrow \sim 7.5$ L) whereas on the top of the images, the total O_2 (H_2) dosage D_{O2} (D_{H2}) after each measurement is mentioned. (g,h) Color coded profiles, with profile (g) and (h) taken from image (b) and (e), respectively. The profiles present the course of the WF after a H_2 pulsec wheras the gray shaded regions in (g) and (h) show the length of a pulse. PdNI growth: 3.3 ML Pd at RT (35% coverage), nc-AFM: $\triangle f$ = -22.0 (a,b), -25.0 (c), -27.0 Hz (d-f).

so that the islands are made from pure Pd[35]. This explains why the islands exhibit a WF difference of +1.09 eV with HOPG in Figure 4a (bottom), which agrees with the expected WF difference of $\triangle\phi_{\text{Pd-HOPG}} \approx +1.1$ eV and which is thanks to the large lateral dimension of the PdNIs and the HOPG regions that keep the tip-surface convolution relatively small. Note that apart from this, the WF difference does not change upon changing the tip-surface distance (see Figure S4 in the Supporting information).

Figure 4a and b show six O_2 and five H_2 pulses (one pulse: ~ 7.5 L) that are sent during the scanning of the surface. As in the PdNP case, an O_2 pulse always increases the WF of the PdNIs (+0.42, +0.34, +0.35, +0.34, +0.29 and +0.29 eV) whereas a following H_2 pulse always decreases the WF (-0.15, -0.11, -0.24, -0.23 and -0.21 eV). As in the PdNP case from above, the WFR takes place upon a H_2 pulse, with H reacting off the pre-adsorbed O forming H_2O that leaves the islands at RT (see discussion section).

After the two measurements shown in Figure 4a and b, a pair of O_2 and H_2 pulses is repeated 13 times on the same islands (Figure 4c-f). As it can be seen by the WF contrast, the trend of the WF increase (decrease) upon an O_2 (H_2) pulse remains the same. However, the absolute values of the WF changes strongly decreases with increasing number of cycles (one cycle is formed by one O_2 and one following H_2 pulse). At the end of the series (Figure 4f), the WF changes are all well below 0.1 eV.

As in the case of the PdNPs from above, the mean WF of the PdNIs increases with increasing number of cycles. An analysis of the initial and final states (Figure S2c,d in the Supporting Information) before and after the overall 19 O_2 and 19 H_2 pulses (total dosages: $D_{O2} = 142.5$ L and $D_{H2} = 142.5$ L) shows that the WF difference between the PdNIs and HOPG has increased by +0.36 eV (from + 1.09 eV onto +1.45 eV).

Note that after the measurement series shown in Figure 4, a 722 L long O_2 exposure does not change the WF of the PdNIs whereas a following 792 L long H_2 exposure decreases the WF by -0.15 eV. The Pd/HOPG system is then completely insensitive upon other O_2 or H_2 exposures, with the WF remaining on a constant value (see Figure S5 in the Supporting

Information).

An other important observation is that at the beginning of the cycling (Figure 4a,b), the WF changes are immediate upon a H_2 pulse. This can be seen by the step-like shape of the profiles in Figure 4g, which show the changes of the WF at the color-coded lines of the image in Figure 4b. However, after many pulses have been sent, e.g., like in Figure 4e, the step-like profile changes to a different shape (Figure 4h): at the beginning of the H_2 pulse, the WF immediately decreases onto a rather constant value. However, as soon as the H_2 pulse is stopped, the WF drifts back onto a saturated value, which is almost half the WF change induced by the H_2 pulse.

O_2 exposure on PdNIs/HOPG. The increase of the mean WF upon several O_2 and H_2 pulses let assume that O is changing Pd in some irreversible way: a) the mean WF that increases by $\sim$+0.4 eV on the PdNIs is close to the value of adsorbed O on Pd(111) (+0.6 eV)[35] and b) adsorbed H does not generally increase the WF of Pd ($<$+0.1 eV at $p_{H2} \approx 10^{-9}$ mbar[23]), in particular not when dissolved in the bulk[23].

To study the impact of O, we show O_2 adsorption KPFM experiments of a third PdNI/HOPG sample, on which the islands exhibit again an expected high WF difference (+1.05 eV) with HOPG (Figure 5). The first 45 L long O_2 pulse in Figure 5a increases the WF of the PdNIs by +0.41 eV (yellow/orange contrast). However, about 10 minutes after the O_2 pulse, the WF has considerably decreased (green contrast) at the upper two NIs (see green arrow). Figure 5b shows another island in the same surface region in this contrast after a second O_2 pulse (not shown). In following images, the same long WF decrease after two O_2 pulses can be observed (Figure 5c,d): at the beginning of a 45 L short pulse, the WF immediately increases by +0.30 and +0.23 but decreases after the pulse on the length scale of minutes. Comparing all O_2 pulses, it can be concluded that the relative WF increase by O decreases with the number of O_2 pulses (+0.41 (a), +0.30 (c), +0.23 (d), and +0.16 eV (e)). The temporal course of the PdNI's WF can be seen in Figure 5i.

After the fourth O_2 pulse (Figure 5e), an about five times longer H_2 pulse (225 L) is sent

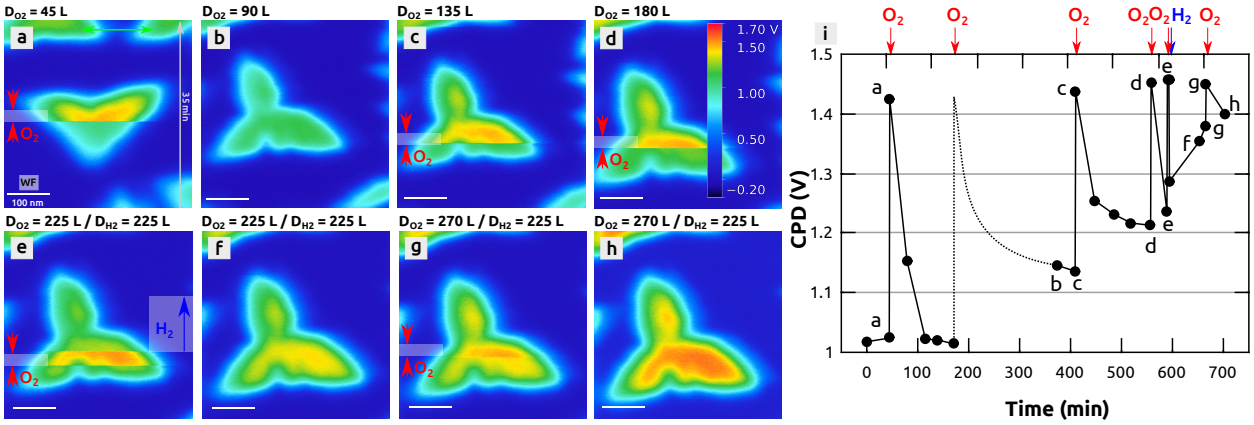

Figure 5: O_2 adsorption KPFM experiments on PdNIs/HOPG with consecutively recorded WF images, which all have the same WF and color scale (a-h). Note that 2 images between image (b) and (c) are not shown, whereas 4 images are not shown between (c) and (d). The red arrows and transparent rectangles mark the length of the pulses. (i) The course of the CPD taken from the images. PdNI growth: 3.3 ML Pd at RT (35% coverage), nc-AFM: $\triangle f$ = -25.0 (a) and -32.0 Hz (b-h).

to test if the WF of the PdNIs can be decreased by H (Figure 5e). Indeed, the WF decreases instantaneously by -0.17 eV at the beginning of the pulse and remains constant until the end of the pulse (Figure 5i). However, this relatively long H_2 pulse does not lead to the initially observed WF value of the PdNIs as observed in Figure 5a (see also Figure 5i). A last 45 L short O_2 pulse does increase the WF, however, only by +0.07 eV (Figure 5g). After a total O_2 dosage of $D_{O2} = 270$ L and additional $D_{H2} = 225$ L of H_2, the PdNIs remain in a constant WF state, exhibiting a WF difference of +1.45 eV with HOPG, which is again +0.4 eV higher than the initial value of +1.05 eV (Figure 5a).

STM during O_2 exposure on PdNIs/HOPG. The decreasing strength of the O induced WF increase upon several O_2 pulses and the related increase of the mean WF of the PdNIs are the same as the ones observed during the cycling of the WFR from above. Obviously, oxygen in whatever form on the Pd facets is the reason for these observations.

We conducted O_2 adsorption STM measurements on a newly prepared PdNI/HOPG sample to study possible structural changes on a smaller length scale compared to the one of

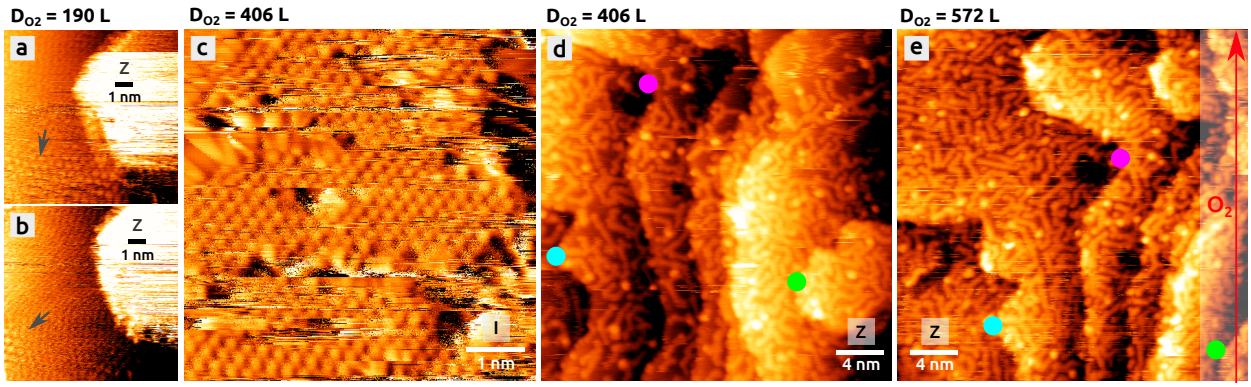

Figure 6: STM images of an O_2 exposed PdNI [(a,b,d,e): topography, (c): current]. (a,b) Images after a 190 L long O_2 pulse (12 min @ 1.5×10^{-7} mbar + 8 min @ 3.0×10^{-7} mbar) with the (2×2) oxygen adsorption structure marked by the arrows. The smaller regular but wavy structure in, e.g., the top parts of both images is due to a periodic noise in the tunnel current. (c) Atomic resolution of the Pd (111) lattice obtained after $D_{O2} = 406$ L of O_2. (d,e) The filament structure on a large scale (d) and during a following O_2 exposure (e). The blue, pink and green dots in both images (d,e) show same surface sites and are a guide to the eye. PdNI growth: 3.3 ML Pd at RT (35% coverage), STM: $I = 0.29$ (a,b), 0.66 (c) and 0.32 nA (d,e), $U_{Bias} = +0.21$ (a,b), $+0.042$ (c) and $+0.50$ V (d,e), $v = 2$ (a,b), 5 (c) and 4 Hz (d,e). Scale: 0.6 nm (a,b), 4 nA (c), 1.1 (d) and 0.8 nm (e).

the previously shown KPFM images (Figure 6). The topography images in Figure 6a,b show a small region of the top facet of one island, after a 190 L long O_2 pulse. Due to the dissociative adsorption of O_2 at RT, a (2×2) adsorption structure is created[30–32]. The (2×2) structure can be seen in the lower part of Figure 6a (see arrow). However, this structure disappears on a time scale of minutes during the scanning (top part of the image) and is almost invisible in Figure 6b: the (2×2) structure can only be seen in the lower left corner in a small region on a Pd terrace (see arrow). Same observations could be done after a few other O_2 pulses up to a total O_2 dosage of $D_{O2} \approx 400$ L. Important to note is that most of the Pd(111) lattice is still intact as it can be seen in the image with atomic resolution (Figure 6c). However, several atomic sized defects are present, together with some features that seem to get moved horizontally by the STM tip along the fast scanning direction.

Figure 6d shows the Pd facet on a larger scale. Apart from the typical Pd terraces, a filament structure can be seen on the terraces. The number of filaments increases during a following, long O_2 pulse (Figure 6e) whereas the filament density saturates at $(6 \pm 3) \times 10^{13}$ filaments/cm^2, after a total O_2 dosage of roughly $\sim$500 L (see Figure S6 in the Supporting Information). Important to note is that a following 260 L long H_2 pulse does not change the filament structure (Figure S6e in the Supporting Information).

The high resolution image in Figure 7a shows the filament structure, after a total O_2 and H_2 dosage of $D_{O2} = 655$ and $D_{H2} = 260$ L, respectively. Note that in some cases, only the atomic structure of the Pd(111) lattice is resolved in STM images without showing the filament structure (Figure S7 in the Supporting Information). However, upon changes of the STM tip, which may appear occasionally even when the scanning parameters remain unchanged, the atomic resolution can be lost at the expense of the filament structure.

A filament has a length between 2 and 3 nm, a width of around 0.6 nm and a distance to the next filament of around 1 nm (Figure 7b). It seems that the filaments are composed of atomic features that are lined up (see green arrow), with a mean distance of (0.53$\pm$0.05) nm, which is about two times the next-next-neighbor Pd distance ($e = a_{Pd} / \sqrt{2} \approx 0.275$ nm, with $a_{Pd} = 0.389$ nm, see Table S3 in the Supporting Information). Although the image quality is relatively low, the density of the atomic features can still be roughly estimated ($\rho_O \approx 2 \times 10^{14}$ atomic features/cm^2, see Figure S8 in the Supporting Information), which is about 13 % of the atomic sites in the ordered Pd (111) lattice ($\rho_{Pd(111)} = 4\sqrt{3} / (3\, a^2_{Pd}) \approx 1.525 \times 10^{15}$ Pd atoms/cm^2). Another important observation is that in some images, the filaments seem to be aligned along the simple crystallographic surface directions of the Pd (111) lattice, forming at some places the typical angles of 60 and 120° when they cross each other (see Figure S8 in the Supporting Information).

For the discussion (see below), we show in Figure 7c the carbon precursor structure, which can be obtained by cracking a small amount of ethylene at around 650 °C on as-prepared PdNPs[27,42]. The latter structure is quite similar to the filament structure observed here and

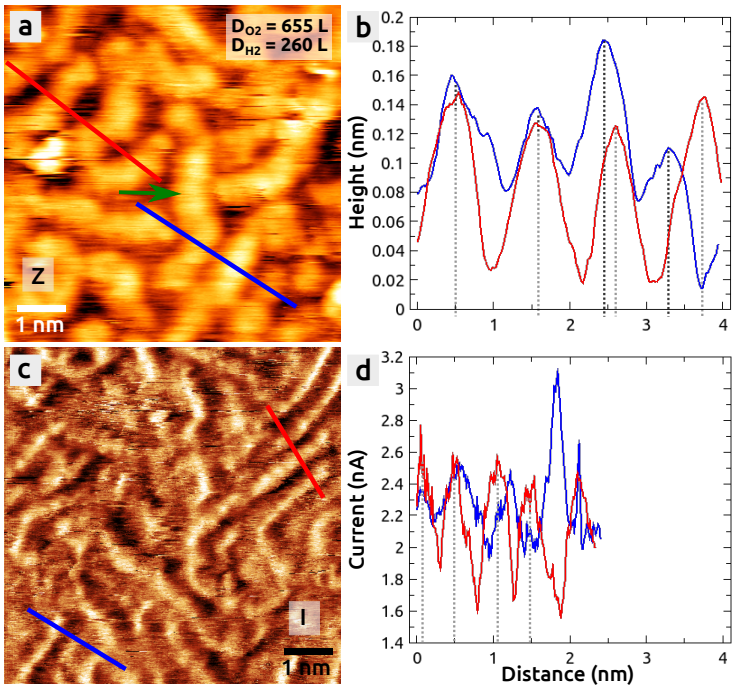

Figure 7: (a) STM image of the filament structure after a total O_2 exposure of $D_{O2} = 655\,L$, in comparison to the carbon precursor structure observed after cracking $D_{C2H4} = 22\,L$ of C_2H_4 at 665 °C on PdNPs (c)[27,42]. Image (a) shows the topography and image (c) the current signal. (b,d) Profiles obtained at the color coded lines shown in (a,c). Growth conditions: 3.3 ML Pd at RT (a) and 1 to 1.5 ML Pd at 480 °C (c), STM: $I = 3.1$ (a) and 2.11 nA (c), $U_{Bias} = +0.021$ (a) and +0.027 V (c), $v = 4$ (a) and 5 Hz (c).

is composed of carbon species with a density of at least $\rho_C \geq \approx 4 \times 10^{14}$ carbon species/cm^2 (see Figure S8 in the Supporting Information), which is roughly two times larger than ρ_O. The higher density of the C filaments influences the mean filament-filament distance, which is smaller in the case of the C filaments compared to the one of the filaments observed in this work (compare the profiles in Figure 7b and d).

XPS after O_2 exposure on PdNIs/HOPG. In Figure 8, two XPS experiments conducted on two newly prepared PdNI/HOPG sample surfaces are shown to state whether or not an oxide in whatever form is created on the PdNIs. The PdNIs are grown in the XPS chamber at RT, using similar Pd quantities (9 and 11 ML) and a similar Pd flux as in the SPM chamber so that same type of PdNIs are obtained [compare STM images in Figure S9 (sample for XPS) with images in Figure S3 (sample for SPM)]. The XPS spectra of the initially clean samples are shown in blue, together with the spectra in red of same samples after 10 consecutive WFR cycles (Figure 8a) and after 5 consecutive O_2 pulses (Figure 8b). Note that almost same parameters for the WFR and O_2 exposure experiments are used as in the experiments shown in Figure 4 (WFR) and Figure 5 (O_2 adsorption). This concerns in particular the $\sim 5.0 \times 10^{-7}$ mbar high partial pressure for O_2 and H_2, the pulse lengths and the pulse delays.

All spectra contain the typical Pd $3d_{3/2}$ and Pd $3d_{5/2}$ peaks at a binding energy of 340.0 and 334.7 eV, respectively, which can be assigned to bulk Pd according to literature (Pd $3d_{3/2}$: 340.6 eV[43], 340.6 eV[24], 340.6 eV[44] and Pd $3d_{5/2}$: 335.3 eV[43], 335.0 eV[24], 335.2 eV[44], 334.9 eV[45]). Most important is that the spectra recorded after the two exposure experiments coincide almost perfectly with the spectra obtained just before so that the difference of the spectra is almost perfectly zero (black curves). As a result of all this, no other peaks can be found after the WFR and oxygen adsorption experiments, in particular not at the binding energy of a peak that can be assigned to PdO (337.0 eV[43], 336.6 eV[24], 336.3 eV[44], 336.4 eV[45], 336.1 eV[46]), with a contribution of only the surface part (approx. at 335.4 eV[44]). Apart from the Pd $3d_{3/2}$ / Pd $3d_{5/2}$ spectrum, there is no detectable change in the Pd Auger MVV lines,

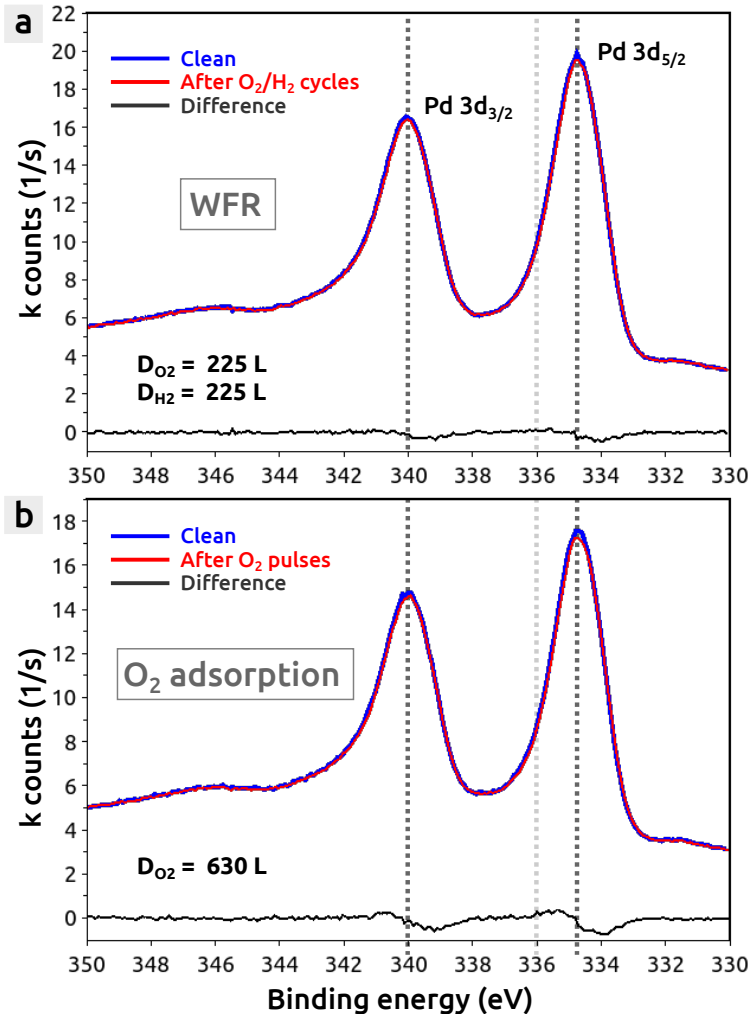

Figure 8: XPS measurements after 10 consecutive O_2 and H_2 cycles with a total dosage of $D_{O2} = D_{H2} = 225\,L$ (pulse delay: 3 min) (a), and after 5 consecutive O_2 pulses with a total dosage of D_{O2} =630 L (pulse delay: 45 min) obtained on a second PdNI/HOPG sample. A partial pressure of $\sim 5.0 \times 10^{-7}$ mbar is used for all pulses whereas the dosage is determined by the length of the pulses (O_2 and H_2 pulses in (a): 22.5 L each, O_2 pulses in (b): 78.8, 78.8, 150, 150, 150 L). The gray dotted lines show the Pd $3d_{3/2}$ and Pd $3d_{5/2}$ peaks at 340.0 and 334.7 eV, respectively, whereas the light gray dotted line shows the position of the expected but missing peaks at ~336 eV for bulk and surface PdO [24,43–46]. PdNI growth: 9 ML (a) and 11 ML Pd (b) at RT.

no change in the valence band, no appearance of an Auger O KVV line either and not a single change in the Pd 3p line with the O1s peak starting to appear[24,43] (see Figure S10 in the Supporting Information).

With help of the program SRD-71[47] and QUASES-IMFP-TPP2M[48,49], an inelastic free mean path l (IFMP) of 1.7 and 1.3 nm, respectively, can be found for the 3d bands of Pd at an electron energy of 930 eV. Using the common assumption that the sampling depth is $3\,l$ (the depth at which 95 % of all electrons are scattered when they reach the surface) and accounting for the detection angle of 53° with respect to the surface normal, the effective sampling depth is estimated between 2.3 nm (SRD-71) and 3.1 nm (QUASES-IMFP-TPP2M), which translates into 10 to 14 atomic layers for an atomic layer distance of $a_{Pd} / \sqrt{3} \approx 0.225$ nm. With this it can be clearly stated that no bulk Pd nor a thin oxide layer with a thickness of a few atomic layers are formed during all exposure experiments discussed in this work.

$O_2 + H_2$ exposure on PdNIs/ceria/Cu(111). In the following, we compare the WFR on the HOPG supported PdNIs with the WFR that can be also observed on same PdNIs, which are grown on a Cu(111) supported, 3 to 4 ML ultra-thin ceria film (Figure 9).

The ultra-thin ceria film is composed by up to 20 nm wide ceria islands, which have a height of either one or two O-Ce-O MLs (Figure 9a). Low energy electron diffraction (LEED) measurements still show the diffraction peaks of the Cu(111) support (see Figure S11a in the Supporting Information), in agreement with STM which shows the uncovered copper support in very small regions of the surface. We estimate that the surface coverage by ceria is at least 95 % high. After the deposition of Pd onto the ceria film at RT, the surface shows more uniform and flat nano-objects compared to before. Those objects are PdNIs (Figure 9b), which have a (111) orientation (see Figure S11b of the Supporting Information) and a mean lateral size of 10 nm. Due to the flat growth and the relatively high deposited amount of Pd (7.0 ML), the PdNIs partially coalesce and exhibit at some places depressions of ∼1.5 nm. The latter value roughly corresponds to the expected island height of ∼1.7 nm for a 7.0 ML closed and flat film, which is calculated from the deposited amount of Pd and the surface

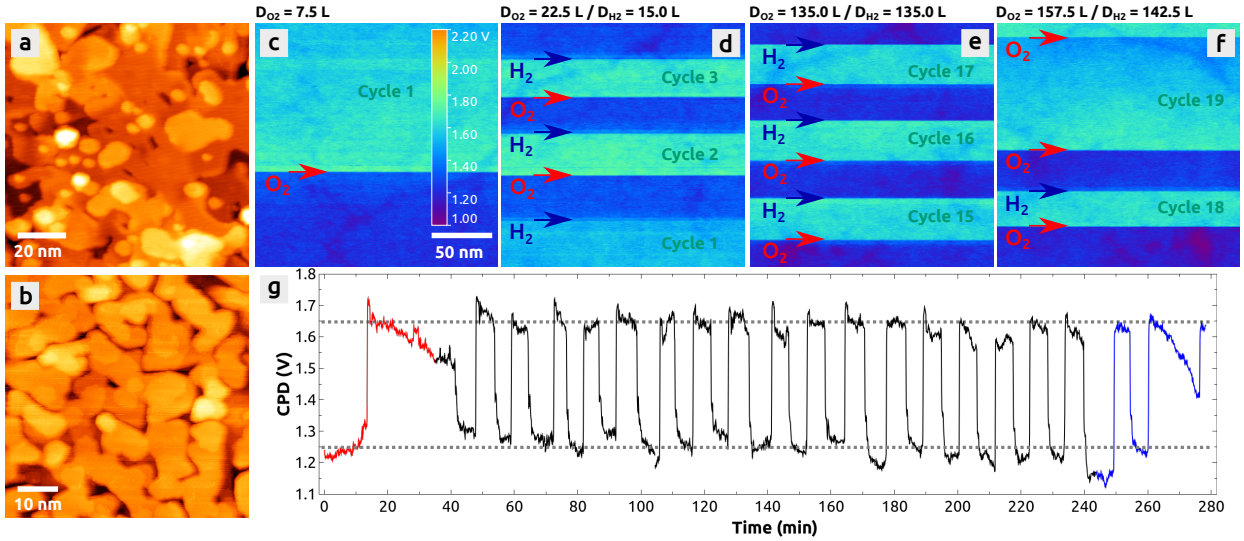

Figure 9: The WFR on PdNIs supported on a 3 to 4 ML ultra-thin ceria film on Cu(111). The STM images (a) and (b) show the clean and Pd covered ceria film, respectively. (c-f) Four selected WF images of an eight-image large image series that can be found in Figure S11 of the Supporting Information. The images show the first 3 (c,d) and the last $4\frac{1}{2}$ of the overall 19 WFR cycles (one O_2 or H_2 pulse: $\sim 5.0 \times 10^{-7}$ mbar, 20 sec $\rightarrow \sim 7.5$ L) (d,f). All WF images have the same color and voltage scale. (g) Temporal course of the CPD during all the 19 WFR cycles obtained in the 8 WF images. The red and blue colored parts of the curve show the temporal development of the CPD after the first and last O_2 pulse. Ceria film growth (>95 % coverage): Ce evaporation with $T_{Sample} < 315$°C + following oxidation at 560°C in 158 L of O_2 (5×10^{-7} mbar), PdNI growth: 7.0 ML Pd at RT (~90% coverage), STM: I = 0.03 nA (a,b), $U_{Bias} = +3.0$ (a) and +0.8 V (b), $v = 3.9$ (a) and 9.8 Hz (b), nc-AFM: $\triangle f$ = -11.9 Hz.

coverage. Support for a closed film comes from KPFM images (see Figure S11c,d in the Supporting Information), which show a uniform surface potential. We estimate a surface covrage of 90%.

In Figure 9c-f, four selected WF images are shown, which are part of an eight-image large image series (see Figure S12 of the Supporting Information). Figure 9c and d present the first WFR cycles whereas images Figure 9e and f show the last $4\frac{1}{2}$ of the overall 19 WFR cycles. Figure 9g shows the temporal course of the CPD during all the 19 WFR cycles whereas changes of the CPD directly reflect the changes of the Pd WF. Note that there is no lateral contrast in the WF images because Pd is covering 90 % of the ceria film.

After the first 7.5 L short O_2 pulse (Figure 4c), the WF of the PdNIs increases by +0.4 eV, which is comparable with the increase observed after the first O_2 pulse on the PdNI/HOPG sample (Figure 4a). After the pulse, the WF decreases during 27 min by roughly 1/3rd of the initial increase (see red curve in Figure 9g), which is comparable with the decrease observed after a O_2 pulse on the PdNI/HOPG sample (Figure 5). When finishing the first WFR cycle with a first 7.5 L short H_2 pulse (at the bottom of Figure 4d), the WF decreases almost onto its initial value. The following two WFR cycles clearly show that the same WF increase and decrease of $\pm$0.4 eV are observed when sending a short O_2 and H_2 pulse, respectively. In strong contrast to the PdNI/HOPG sample, the WF change of $\pm$0.4 eV does not change when passing 15 (Figure 4e) and even 19 WFR cycles (Figure 4f), as also shown in the graph of Figure 4g. Even the temporal decrease of the WF after the last O_2 pulse is reproduced (blue part of the curve in Figure 4f).

DISCUSSION

In the following, we focus on the PdNIs and refer to the PdNPs if necessary.

The WFR as Observed by KPFM. All previous literature work shows that O_2 and H_2 dissociatively adsorb on Pd(111) [23,24] and that they form water, which leaves immediately

the PdNIs facets at RT[10,11,15]. As long as H_2O is produced, no H_2 is formed and all the OH is also immediately consumed[15]. Note that because we study the WFR and oxygen adsorption at RT, we clearly exclude a bulk Pd oxide formation but also a thin oxide layer with a thickness of a few atomic atomic layers, as evidenced by our XPS measurements and shown by previously published work: a bulk oxide with nanometer thickness is created under an atmospheric O_2 pressure and at temperatures higher than 650 °C[43] whereas a surface oxide with a thickness of a few Ångströms is formed at O_2 partial pressures higher than 10^{-6} mbar and still at temperatures higher than 200 °C[31,45,50], which is also the case for PdNPs[4].

Under our low pressure ($<1 \times 10^{-6}$ mbar) and RT conditions, we assume that O adsorbs only in the well known (2×2) adsorption structure[30–32] and that no higher O coverages are reached at RT, unlike the case when, e.g., NO_2 is dosed[24]. Note that in the latter case, a shoulder close to the Pd $3d_{3/2}$ and Pd $3d_{5/2}$ peaks should have been observed by our XPS, pointing to a surface oxide[24], which is, however, not the case here.

Oxygen in the (2×2) adsorption structure is located in threefold sites and increases the WF by more than +0.5 eV[33,35], whereas H also increases the WF but much less: classical Kelvin probe yields a WF change of about +0.10 and +0.16 eV when H_2 is constantly dosed with a partial pressure of $p_{H2} \approx 1 \times 10^{-9}$ and 5×10^{-7} mbar[23], respectively, which is in agreement with calculations that consider H to be on the surface[51]. From these considerations it follows that a WF decrease of at least -0.3 eV is expected when H entirely reacts off the preadsorbed O.

And indeed, with respect to Pd/HOPG, we observe a quick strong WF increase of +0.4 eV after the first O_2 pulse and an immediate step-like WF decrease with a similar but smaller strength after the following H_2 pulse (Figure 4a). We can therefore assign the WF changes to the WFR between O and H. This first WFR cycle can be repeated up to three times on the PdNIs and two times on the PdNPs, without almost no changes of the mean Pd WF.

The WFR can be also observed on the ultra-thin ceria film supported PdNIs: the same WF changes of ±0.4 eV are observed upon a short O_2 and H_2 pulse. However, in strong

contrast to the Pd/HOPG case, the WF changes remain constant and no change of the PdNI's mean WF is observed. In other words, the WFR can be cycled a dozen of times without any signatures of a deactivation process of the WFR, as it seems to be the case for Pd/HOPG. Note that a relatively small amount of H_2 (effective dosage: $7.5\,\mathrm{L} \,/\, 0.44 = 17.0\,\mathrm{L}$) is needed to react off the entire oxygen from the Pd. Note that the effective O_2 dosage of 8.6 L (7.5 L / 0.87) already leads to an almost complete saturation of oxygen on Pd(111) [33].

Before we discuss the deactivation of the WFR on the Pd/HOPG catalyst, we comment the temporal course of the WF after an O_2 pulse is sent: on both catalysts, we observe a WF decrease on a time scale of a few 10 minutes (Figure 5 and Figure 9) and also a disappearance of the (2×2) adsorption structure by STM (Figure 6a,b). This means that the O, which is already mobile at 200 K on Pd(111) [32], has to leave the facets and move by time to some other places. We almost entirely exclude that a part of the O slowly recombines to gas-phase O_2 on the Pd because the O_2 desorption peak is located above 470 °C [30,54,55]. We also exclude an O diffusion into subsurface regions, which starts to appear at higher coverages of around 0.5 [52], but also because subsurface O would invert the surface dipole, strongly decreasing the WF, which we, however, never observed. A possible mechanism could be based on dissolved H, which back-diffuses to the surface, recombining with the adsorbed O to gas-phase H_2O, as observed before at low temperatures [53]. Although we cannot exclude such H back-diffusing after several H_2 pulses have been sent during cycling the WFR, it does not explain the oxygen removal in the O_2 adsorption experiments in Figure 5. As the only suspect remains H_2 from the residual gas of the UHV, which is reacting off the oxygen: indeed, on the Pd/ceria/Cu(111) catalyst, the pressure decreased within some minutes onto 9×10^{-10} mbar after the first O_2 pulse (red curve in Figure 9g), and after 27 minutes an effective $\sim$3 L large dosage of the residual gas that contains mostly H_2 is reached. Because we just noticed above that 17 L of H_2 are needed to react off a saturated O layer on Pd it is clear that, after an O_2 pulse, a few 10 minutes lasting WF decrease of 1/3rd can be assigned to 3 L of H_2 from the residual gas of the UHV. The same certainly applies to the WF decrease visible in Figure 9g

(blue curve) and on Pd/HOPG in Figure 5.

The support effect on the WFR. The comparison with the Pd/ceria/Cu(111) catalyst clearly shows that the support has obviously an effect on the WFR. STM on the PdNI/HOPG shows furthermore that an irreversible filament structure is formed, which is responsible for the decreasing strength of the WF changes and the increasing mean WF of the PdNIs after several WFR cycles have been executed. A comparison of this filament structure with the previously observed carbonic precursor structure[27,42] reveals striking similarities (Figure 7c). We can therefore strongly anticipate that obviously the carbon from the graphite plays an important role in the WFR on Pd/HOPG samples. In the following, we postulate a possible model of the Pd/HOPG catalyst deactivation.

If it is assumed that carbon is included in the filament structure on the PdNIs, the carbon has to be detached from the graphite. This is only possible during a hydrogenation of the graphite to CH_4[56–58] and/or an oxidation of the graphite to CO_2[59,60], during which a certain amount of C is left at the Pd facets and used for the filament creation. Indeed, metal NPs have the tendency to etch the steps of graphite and edges of graphene upon hydrogenation, as shown with NiNPs[56], FeNPs[57] and CoNPs[58]. However, the etching is observed at high temperatures (NiNPs: 750 to 1100 °C, FeNPs: 900 °C, CoNPs: 600 °C) and high partial pressures so far (some mbar and more). High temperatures (>440 °C) and pressures of some mbar[59] or in the 10^{-6} mbar range[41] are also used for the oxidation of the graphite.

During such hydrogenation and oxidation experiments, the metal NPs create large pits and also long channels inside the graphite/graphene material, which shows that a *very large C quantity* is detached from the graphite. For instance, more than 100 nm long and up to 2 nm deep channels are created by PdNPs during an dosage of only $p_{O2} = 5 \times 10^{-6}$ mbar O_2 at 500 °C[41].

Compared to the latter large C quantity, the C amount required for the creation of the carbonic precursor structure in Figure 7c is much less: only about 20 L of C_2H_4 are needed[27,42]. Therefore, if C detachment appears during a possible hydrogenation or oxidation

of the graphite, the temperature can be probably much lower than mentioned above, just to detach a *small amount of C only*. In view of this it is important to note that when growing PdNPs at only 150 °C on HOPG, a small amount of C is included in subsurface positions below the NP's facets[27].

We stress here that the catalyst's local temperature is increased during the oxidation of the graphite: an increase of $\triangle T \approx 150$ °C was observed for PdNPs on HOPG[60], which raises the otherwise too low sample temperature to a higher, *local temperature* being close to the Tammann temperature, at which the PdNPs can move and create the channels in the graphite[41]. An increase of the catalyst's local temperature certainly appears also in the hydrogenation of graphite, the dissociative adsorption of O_2 and H_2 and in particular during the water forming step, which the latter releases a large energy in form of local heat. Such a local temperature increase could possibly explain why a small amount of C can be indeed detached from the graphite in our experiments.

Due to the reasons from above we assume that a small amount of graphite released C is located either in subsurface positions below the Pd facets[27] or rather on the facets creating a filament structure, as we have recently described[42]. However, it is clear that this filament structure cannot be made from C alone but must be rather a mixture together with O and H since the PdNIs are exposed to O_2 and H_2 in our WFR experiments (only O in oxygen adsorption experiments). A strong signature comes from the relatively low WF difference between the carbon precursor structure on PdNPs and the graphite support (+0.4 eV)[27], which is about 1.0 eV lower than the WF difference observed here on the PdNIs (+1.4 eV). We therefore assume that O_2 dissociatively adsorbs on the Pd facets and that it then bounds to C induced defects in the first atomic Pd layer[27] since we could observe defects appearing in the Pd(111) lattice (Figure 6c). Even more, we do not rule out the possibility that some adsorbed CO is formed, which the latter also strongly increases the WF of Pd(111) by more than +1.0 eV at RT[61]. In both cases, the adsorbed O or CO species would be then more strongly bound to the Pd facets so that no H can react off anymore the O. In other words,

the Pd catalyst is deactivated.

Interestingly, the WFR seems to get more quickly deactivated on PdNPs (starting at ∼50 L, Figure 3) compared to the deactivation of the WFR on PdNIs (starting at ∼150 L, Figure 4). We speculate that this might be due to the subsurface carbon already included in the PdNPs and also due to the smaller size of the NPs compared to the NIs.

CONCLUSIONS

We show that by using Kelvin probe force microscopy (KPFM), the water forming reaction (WFR) between atomic O and H can be well characterized at room temperature (RT) and under UHV conditions on Pd nanoislands (PdNI) and nanoparticles (PdNP), which are grown in their (111) epitaxy on HOPG and Cu(111) supported ultra-thin cerium oxide (ceria) films: when sequentially pulsing O_2 and H_2 within a WFR cycle, KPFM exhibits a WF increase of +0.4 eV upon a ∼5 L short O_2 pulse ($p_{O2} \approx 5 \times 10^{-7}$ mbar), which is due to the oxygen (2×2) adsorption structure on Pd(111). A following short H_2 pulse immediately leads to a complete WF reduction, which is due to the H that reacts off the entire O by forming gas-phase H_2O. KPFM shows here its clear advantage over standard topography imaging, making such a catalytic reaction visible thanks to its potential to measure related WF changes at the nanometer length scale and also in dependence on time. It is a promising supplementary SPM technique in heterogeneous catalysis that can be used in future for studying any catalytic reaction at metal NPs.

With increasing number of WFR cycles, a new phenomenon is observed on the Pd/HOPG catalyst: the relative strength of the WF changes that appear upon the short O_2 or H_2 pulses strongly decreases because of an irreversible increasing *mean WF* of the PdNIs (PdNPs). The mean WF almost reaches the value of the (2×2) oxygen adsorption structure, which is observed also in only O_2 adsorption experiments. Responsible for the mean WF increase is an increasing number of nanometer sized filaments that appear on the facets, covering ∼10%

of the Pd (111) lattice. Assisting XPS does not show any signatures of a nanometer thin PdO film or a surface oxide, pointing to some *on-top* adsorbed O that is either undetectable with our XPS or desorbed during the long X-ray acquisition time. In strong contrast to the Pd/HOPG catalyst, the WFR can be followed on the Pd/ceria catalyst during an unlimited number of WFR cycles during which the strength of the WF changes remains constant.

The comparison clearly shows that the HOPG support plays an important role in the WFR. We postulate that due to the dissociative O_2 and H_2 adsorption, O and H are used for a hydrogenation and oxidation of the graphite, respectively, which both also release a small amount of C into the Pd. The adsorbed O is then bound either to C induced defects in the first atomic Pd layer or it forms with C adsorbed CO, in the presence of also H. The resulting filament structure deactivates then the Pd/HOPG catalyst. No such a deactivation is observed on Pd/ceria because the catalyst is carbon-free.

In future, oxygen and also CO + hydrogen adsorption experiments followed by low temperature STM/nc-AFM with atomic resolution in conjunction with density functional theory (DFT) could be done to identify the detailed atomic structure and precise composition of the filament structure.

ACKNOWLEDGMENTS

Support from the *Agence Nationale de la Recherche* (ANR) through project *REACTIVITY* (grant ANR-17-CE09-0045) is gratefully acknowledged.

ASSOCIATED CONTENT

Supporting Information. Details about STM, nc-AFM, KPFM and XPS as well as about the sample preparation and material properties (PDF), and supporting SPM and XPS measurements.

AUTHOR INFORMATION

Corresponding Author

E-mail: barth@cinam.univ-mrs.fr

ORCID

Baptiste Chatelain: 0000-0003-3121-0409

Ali El Barraj: 0000-0002-9947-6935

Carine Laffon: 0000-0001-7060-3833

Philippe Parent: 0000-0002-6229-6471

Clemens Barth: 0000-0003-4250-4533

Author Contributions

B. C., A. E. B. and C. B. conducted and analyzed the SPM experiments whereas B. C., C. L. and P. P. conducted and analyzed the XPS experiments. C. B. wrote the manuscript.

Funding Sources

Agence Nationale de la Recherche (ANR-17-CE09-0045, project *REACTIVITY*).

Notes

The authors declare no competing financial interests.

References

1. Collins, P. M. D. The Pivotal Role of Platinum in the Discovery of Catalysis. *Platin. Met. Rev.* **1986**, *30*, 141–146.

2. Völkening, S.; Bedürftig, K.; Jacobi, K.; Wintterlin, J.; Ertl, G. Dual-Path Mechanism for Catalytic Oxidation of Hydrogen on Platinum Surfaces. *Phys. Rev. Lett.* **1999**, *83*, 2672–2675.

3. Trinchero, A.; Hellman, A.; Grönbeck, H. Methane Oxidation Over Pd and Pt Studied by DFT and Kinetic Modeling. *Surf. Sci.* **2013**, *616*, 206–213.

4. Matsumura, D.; Taniguchi, M.; Tanaka, H.; Nishihata, Y. In Situ X-Ray Absorption Spectroscopy Study on Water Formation Reaction of Palladium Metal Nanoparticle Catalysts. *Int. J. Hydrogen Energy* **2017**, *42*, 7749–7754.

5. Mitchell, G. E.; White, J. M. Identification of the Intermediate in the Water Formation Reaction on Pt(111). *Chem. Phys. Lett.* **1987**, *135*, 84–88.

6. Anton, A. B.; Cadogan, D. C. The Mechanism and Kinetics of Water Formation on Pt(111). *Surf. Sci.* **1990**, *239*, L548–L560.

7. Koch, M.H.; Jakob, P.; Menzel, D. The Influence of Steps on the Water-Formation Reaction on Ru(001). *Surf. Sci.* **1996**, *367*, 293–306.

8. Nyberg, C.; Tengstål, C. G. Adsorption and Reaction of Water, Oxygen, and Hydrogen on Pd(100): Identification of Adsorbed Hydroxyl and Implications for the Catalytic H_2-O-O_2 Reaction. *J. Chem. Phys.* **1984**, *80*, 3463–3468.

9. Nyberg, C.; Uvdal, P. The Oxygen-Water Reaction on Pd(100): Observation of a Precursor Complex. *J. Chem. Phys.* **1986**, *84*, 4631–4635.

10. Engel, T.; Kuipers, H. A Molecular-Beam Investigation of the Reaction H_2 + 1/2 O_2 => H + 1/2 O_2 => H_2O on Pd(111). *Surf. Sci.* **1979**, *90*, 181–196.

11. Pauer, G.; Winkler, A. Water Formation on Pd(111) by Reaction of Oxygen with Atomic and Molecular Hydrogen. *J. Chem. Phys.* **2004**, *120*, 3864–3870.

12. Piccolo, Laurent; Piednoir, Agnès; Bertolini, Jean-Claude Absorption and Oxidation of Hydrogen at Pd and Pd-Au (111) Surfaces. *Surf. Sci.* **2006**, *600*, 4211–4215.

13. Winkler, A.; Kratzer, M.; Pauer, G.; Eibl, C.; Gleispach, D. Time-of-Flight Studies on Catalytic Model Reactions. *Top. Catal.* **2007**, *46*, 189–199.

14. Weissman-Wenocur, D. L.; Spicer, W. E. Comparison Between the Catalytic Activities of Pd(111) and Pd-Au(111) for Water Synthesis. *Surf. Sci.* **1983**, *133*, 499–515.

15. Mitsui, T.; Rose, M. K.; Fomin, E.; Ogletree, D. F.; Salmeron, M. Coadsorption and Interactions of O and H on Pd(111). *Surf. Sci.* **2002**, *511*, 259–266.

16. Mitsui, T.; Rose, M. K.; Fomin, E.; Ogletree, D. F.; Salmeron, M. A Scanning Tunneling Microscopy Study of the Reaction Between Hydrogen and Oxygen to Form Water on Pd(111). *J. Chem. Phys.* **2002**, *117*, 5855–5858.

17. Johansson, Å; Försth, M.; Rosén, A. A Comparative Study of High-Temperature Water Formation and OH Desorption on Polycrystalline Palladium and Platinum Catalysts. *Surf. Sci.* **2003**, *529*, 247–266.

18. Pauer, G.; Kratzer, M.; Winkler, A. Reaction and Desorption Kinetics of H_2 and H_2O on Activated and Non-Activated Palladium Surfaces. *Vacuum* **2005**, *80*, 81–86.

19. Petersson, L. -G.; Dannetun, H. M.; Lundström, I. Hydrogen Detection During Catalytic Surface Reactions: Evidence for Activated Lateral Hydrogen Mobility in the Water-Forming Reaction on Pd. *Phys. Rev. Lett.* **1984**, *52*, 1806–1809.

20. Fogelberg, J.; Petersson, L.-G. Kinetic Modelling of the H_2-O-O_2 Reaction on Pd and of its Influence on the Hydrogen Response of a Hydrogen Sensitive Pd Metal-Oxide-Semiconductor Device. *Surf. Sci.* **1996**, *350*, 91–102.

21. Cao, Y.; Chen, Z.-X. Theoretical Studies on the Adsorption and Decomposition of H_2O on Pd(111) Surface. *Surf. Sci.* **2006**, *600*, 4572–4583.

22. Petrauskas, V.; Tornau, E. E. Simulation of Hydrogen-Induced Reconstruction of Oxygen on Pd(111). *Acta Phys. Pol. A* **2008**, *113*, 1075–1078.

23. Conrad, H.; Ertl, G.; Latta, E. E. Adsorption of Hydrogen on Palladium Single Crystal Surfaces. *Surf. Sci.* **1974**, *41*, 435–446.

24. Banse, B. A.; Koel, B. E. Interaction of Oxygen with Pd(111): High Effective O_2 Pressure Conditions by Using Nitrogen Dioxide. *Surf. Sci.* **1990**, *232*, 275–285.

25. Andersson, M.; Rosén, A. Adsorption and Reactions of O_2 and D and D_2 on Small Free Palladium Clusters in a Cluster-Molecule Scattering Experiment. *J. Phys. Condens. Matter* **2010**, *22*, 334223.

26. Eriksson, M.; Hultman, L.; Petersson, L.-G. The Water-Forming Reaction on Thin, SiO_2 Supported, Palladium Films. *Vacuum* **1990**, *41*, 137–138.

27. Grönbeck, H.; Barth, C. Revealing Carbon Phenomena at Palladium Nanoparticles by Analyzing the Work Function. J. Phys. Chem. C. *J. Phys. Chem. C* **2019**, *123*, 4360–4370.

28. Albers, P.; Pietsch, J.; Parker, S. F. Poisoning and Deactivation of Palladium Catalysts. *J. Mol. Catal. A* **2001**, *173*, 275–286.

29. Argyle, M.; Bartholomew, C. Heterogeneous Catalyst Deactivation and Regeneration: A Review. *Catalysts* **2015**, *5*, 145–269.

30. Conrad, H.; Ertl, G.; Küppers, J.; Latta, E. E. Interaction of NO and O_2 with Pd(111) Surfaces. II. *Surf. Sci.* **1977**, *65*, 245–260.

31. Zheng, G.; Altman, E. I. The Oxidation of Pd(111). *Surf. Sci.* **2000**, *462*, 151–168.

32. Rose, M. K.; Borg, A.; Dunphy, J. C.; Mitsui, T.; Ogletree, D. F.; Salmeron, M. Chemisorption of Atomic Oxygen on Pd(111) Studied by STM. *Surf. Sci.* **2004**, *561*, 69–78.

33. Surnev, L.; Bliznakov, G.; Kiskinova, M. Oxygen Adsorption on a Pd(111) Surface. *Surf. Sci.* **1984**, *140*, 249–260.

34. Petersson, L.-G.; Dannetun, H. M.; Lundström, I. The Water-Forming Reaction on Palladium. *Surf. Sci.* **1985**, *161*, 77–100.

35. Grönbeck, H.; Barth, C. J. Oxygen Adsorption on Graphene Encapsulated Palladium Nanoparticles Imaged by Kelvin Probe Force Microscopy. Phys. Chem. C. *J. Phys. Chem. C* **2019**, *123*, 24615–24625.

36. Ulbricht, H.; Zacharia, R.; Cindir, N.; Hertel, T. Thermal Desorption of Gases and Solvents From Graphite and Carbon Nanotube Surfaces. *Carbon* **2006**, *44*, 2931–2942.

37. Kitamura, S.; Suzuki, K.; Iwatsuki, M. High Resolution Imaging of Contact Potential Difference Using a Novel Ultrahigh Vacuum Non-Contact Atomic Force Microscope Technique. *Appl. Surf. Sci.* **1999**, *140*, 265–270.

38. El Barraj, A.; Chatelain, B.; Barth, C. High-Temperature Oxidation and Reduction of the Inverse Ceria/Cu(111) Catalyst Characterized by LEED, STM, nc-AFM and KPFM. *J. Phys: Condens. Mat.* **2022**, *34*, 014001.

39. Gasperi, G.; Luches, P.; Barth, C. Stability of Ultrathin Ceria Films on Pt(111) Exposed to Air and Treated in Redox Cycles. *J. Phys. Chem. C* **2018**, *122*, 25954–25963.

40. Nakao, F. Determination of the Ionization Gauge Sensitivity Using the Relative Ionization Cross-Section. *Vacuum* **1975**, *25*, 431–435.

41. Palacios-Lidon, E.; Henry, C. R.; Barth, C. Kelvin Probe Force Microscopy in Surface Chemistry: Reactivity of Pd Nanoparticles on Highly Oriented Pirolytic Graphite. *ACS Catal.* **2014**, *4*, 1838–1844.

42. Barth, C. J. Phys. Chem. C. Carbon Precursor Structures and Graphene on Palladium Nanoparticles. *J. Phys. Chem. C* **2018**, *122*, 522–529.

43. Peuckert, M. XPS Study on Surface and Bulk Palladium Oxide, its Thermal Stability, and a Comparison with Other Noble Metal Oxides. *J. Phys. Chem.* **1985**, *89*, 2481–2486.

44. Bondzie, V. A.; Kleban, P.; Dwyer, D. J. XPS Identification of the Chemical State of Subsurface Oxygen in the O/Pd(110) System. *Surf. Sci.* **1996**, *347*, 319–328.

45. Voogt, E. H.; Mens, A. J. M.; Gijzeman, O. L. J.; Geus, J. W. Adsorption of Oxygen and Surface Oxide Formation on Pd(111) and Pd Foil Studied with Ellipsometry, LEED, AES and XPS. *Surf. Sci.* **1997**, *373*, 210–220.

46. Brun, M.; Berthet, A.; Bertolini, J.C XPS, AES and Auger Parameter of Pd and PdO. *J. Electron Spectros. Relat. Phenomena* **1999**, *104*, 55–60.

47. NIST Electron Inelastic-Mean-Free-Path Database: Version 1.2, National Institute of Standards and Technology (NIST), Gaithersburg, USA.

48. QUASES-IMFP-TPP2M: Version 3.0, University of Southern Denmark, Odense, Denmark.

49. Tanuma, S.; Powell, C. J.; Penn, D. R. Calculations of Electron Inelastic Mean Free Paths. V. Data for 14 Organic Compounds Over the 50-2000 eV Range. *Surf. Inter. Anal.* **1994**, *21*, 165–176.

50. Klikovits, J.; Napetschnig, E.; Schmid, M.; Seriani, N.; Dubay, O.; Kresse, G.; Varga, P. Surface Oxides on Pd(111): STM and Density Functional Calculations. *Phys. Rev. B* **2007**, *76*, 045405.

51. Dong, W.; Ledentu, V.; Sautet, Ph.; Eichler, A.; Hafner, J. Hydrogen Adsorption on Palladium: A Comparative Theoretical Study of Different Surfaces. *Surf. Sci.* **1998**, *411*, 123–136.

52. Todorova, M.; Reuter, K.; Scheffler, M. Density-Functional Theory Study of the Initial Oxygen Incorporation in Pd(111). *Phys. Rev. B* **2005**, *71*, 195403.

53. Mitsui, T.; Rose, M.K.; Fomin, E.; Ogletree, D.F.; Salmeron, M. Hydrogen Adsorption and Diffusion on Pd(111). *Surf. Sci.* **2003**, *540*, 5–11.

54. Klötzer, B.; Hayek, K.; Konvicka, Ch.; Lundgren, E.; Varga, P. Oxygen-Induced Surface

Phase Transformation of Pd(111): Sticking, Adsorption and Desorption Kinetics. *Surf. Sci.* **2001**, *482-485*, 237–242.

55. Kan, H. H.; Weaver, J. F. Mechanism of PdO Thin Film Formation During the Oxidation of Pd(111). *Surf. Sci.* **2009**, *603*, 2671–2682.

56. Ci, L.; Xu, Z.; Wang, L.; Gao, W.; Ding, F.; Kelly, K. F.; Yakobson, B. I.; Ajayan, P. M. Controlled Nanocutting of Graphene. *Nano Res.* **2008**, *1*, 116–122.

57. Datta, S. S.; Strachan, D. R.; Khamis, S. M.; Johnson, A. T. C. Crystallographic Etching of Few-Layer Graphene. *Nano Lett.* **2008**, *8*, 1912–1915.

58. Schäffel, F.; Warner, J. H.; Bachmatiuk, A.; Rellinghaus, B.; Büchner, B.; Schultz, L.; Rümmeli, M. H. Shedding Light on the Crystallographic Etching of Multi-Layer Graphene at the Atomic Scale. *Nano Res.* **2009**, *2*, 695–705.

59. Baker, R. T. K.; France, J. A.; Rouse, L.; Waite, R. J. Catalytic Oxidation of Graphite by Platinum and Palladium. *J. Catal.* **1976**, *41*, 22–29.

60. Baker, R. T. K. The Relationship Between Particle Motion on a Graphite Surface and Tammann Temperature. *J. Catal.* **1982**, *78*, 473–476.

61. Ertl, G.; Koch, J. Adsorption von CO auf einer Palladium(111)-Oberfläche. *Z. Naturforsch. A* **1970**, *25*, 1906–1911.

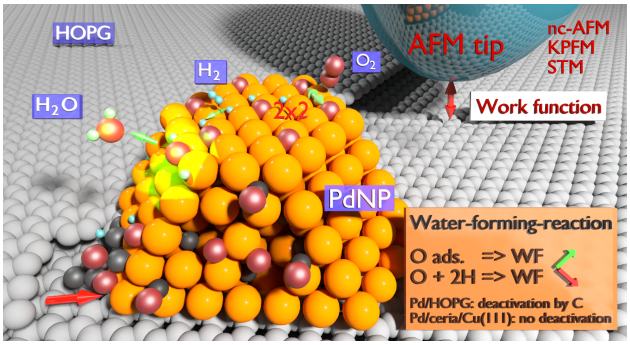
HOPG
H2
O2
H2O
2x2
AFM tip
nc-AFM
KPFM
STM
Work function
PdNP
Water-forming-reaction
O ads. => WF
O + 2H => WF
Pd/HOPG: deactivation by C
Pd/ceria/Cu(111): no deactivation

TOC Graphic